

# A micromachined cochlear-like acoustic sensor

Robert D. White, and Karl Grosh

Department of Mechanical Engineering  
University of Michigan  
Ann Arbor, MI 48109-2125

## ABSTRACT

The mammalian cochlea achieves remarkable acoustic transduction characteristics in a compact and robust design. For this reason, its mechanics have been extensively studied, both mathematically and experimentally. Recently, a number of researchers have attempted to mimic the cochlear function of the basilar membrane in micromachined mechanical devices. This paper presents a design for a silicon cochlea which extends previous work by utilizing a micromachined liquid-filled two duct structure similar to the duct structure of the biological cochlea. Design issues related to both mechanical structure and electrical transduction will be discussed, particularly with regard to optimization of transducer performance. A parallel beam array structure is proposed as a model for an orthotropic membrane. Fabrication procedures and results are also presented. Challenging fabrication issues related to through-wafer etching, adhesive wafer bonding, device release, and fluid injection are emphasized.

**Keywords:** cochlea, micromachined, silicon, transducer, MEMS, acoustic, wafer bonding, DRIE, fluidic, piezoresistor

## 1. INTRODUCTION

The biological cochlea consists of a series of curved, fluid-filled ducts separated by membrane structures. (see Figure 1) One such membrane, the basilar membrane, has mechanical properties which vary along the length of the duct. Due to these varying properties, an incoming acoustic wave induces amplified membrane motion at a specific location along the length of the duct. This motion, through the fluid, stimulates the inner hair cells which send information to the brain. This mechanism creates a sensitive real time frequency analyzer, delivering approximately 3000 channels of frequency information. The human cochlea operates over a 3 decade band in frequency, 120 dB of dynamic range, and can distinguish tones which differ by less than 0.5%.<sup>1,2</sup>

It is these attractive transduction characteristics which motivate imitation. In particular, cochlear-like transduction offers a low-power option for real time mechanical signal analysis.<sup>3</sup> Design and fabrication of cochlear models will also lead to a better understanding of the biological cochlea, with positive impacts in medicine.

Other researchers have fabricated micromachined devices which mimic aspects of the cochlea. Two such devices, the "fishbone" structure reported by Tanaka, Harada, Ando, et al.,<sup>4,5</sup> and the microelectromechanics-based frequency signature sensor(MEM-FSS) reported by Haronian and MacDonald,<sup>6</sup> consist of arrays of beams oscillating in air. Both of these devices are successful at producing cochlear-like acoustic localization. In Tanaka's work, piezoresistive transduction is incorporated. Lim, Steele, et al. report a cochlear-like transducer operating in fluid which utilizes an isotropic silicon nitride membrane.<sup>7</sup> This device uses a macroscale duct structure into which the micromachined membrane is clamped.

The device reported in this paper differs from previous work by utilizing a beam array structure as a model of an orthotropic plate, and by demonstrating a process for achieving a fully micromachined liquid-filled two-duct structure. These features allow this mechanical model to directly capture two important cochlear properties: plate orthotropy and liquid-structure interaction.

This paper briefly presents the modeling techniques used for device design. Structural and transducer design optimization are discussed. Challenges and modeling questions related to beam-array structures are presented, along with a brief discussion of macroscale experiments on such structures. It is argued that a strongly orthotropic plate model can be captured using an array of closely spaced beams. A discussion of microfabrication procedures follows, demonstrating successful mechanical structure fabrication. The challenging aspects of through-wafer etching, adhesive bonding, structure release, fluidic filling, and sealing operations are highlighted.

## 2. DESIGN

### 2.1. Mechanical Model

For modeling purposes, the cochlea can be unwrapped and considered as two rectangular, fluid-filled ducts separated by a flexible membrane structure corresponding to the basilar membrane. (see Figure 1) By allowing the mechanical or geometric properties of the membrane to vary as a function of position down the duct, many of the essential filtering characteristics of the passive biological cochlea can be reproduced.<sup>2,8-11</sup>

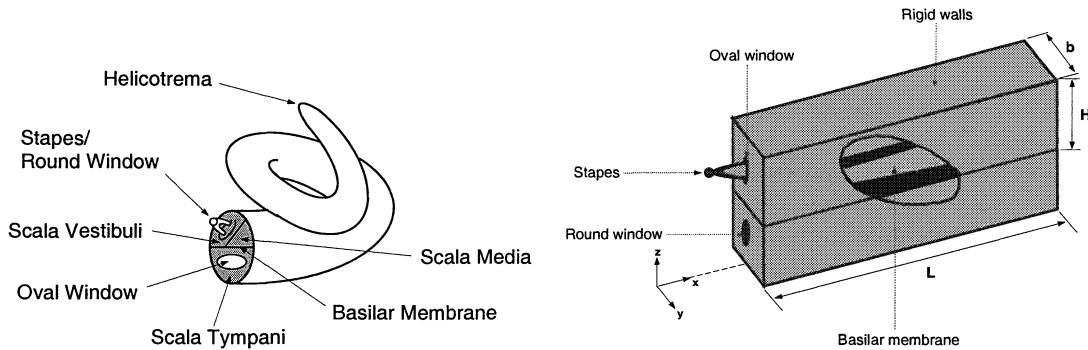


**Figure 1:** The cochlea: (a)Representation of the biological cochlea. (b)Unwrapped two-duct idealized model.<sup>2</sup>

Mathematically, the two-duct coupled problem involves models of both fluid and plate response, and appropriate coupling expressions. The designs discussed in this paper made heavy use of the analytical models discussed in Steele<sup>8</sup> and Parthasarathi.<sup>2,12</sup> These models assume an incompressible fluid with viscous effects included in a thin region near the flexible plate. The plate is modeled as a linear orthotropic Kirchoff plate, and interaction between the plate and fluid is governed by the linearized Euler equation. Details of the modeling methods can be found in the references.

The WKB (Wentzel, Kramer, Brillouin) method can be used to solve equations of this sort where parameters vary slowly compared to the wavelength of oscillations. An oscillatory solution for the plate response is assumed, with slowly varying amplitude and phase. Using this, expressions for the total system energy can be produced in terms of the varying plate amplitude,  $W(x)$ , and complex wavenumber,  $k_x(x)$ . By minimizing variations of the energy with respect to each of these functions, plate response can be determined. Reflected waves from the end of the duct can also be incorporated into the final solution, by requiring that the fluid pressure drop to zero (pressure release) at the apical end of the duct. The advantage of using WKB is that it provides insight into wave propagation along the plate and is computationally efficient. Figure 2 gives two examples of solutions computed in this manner, demonstrating the localization of acoustic energy to different membrane positions depending on the input frequency. It is this type of acoustic energy localization that this transducer attempts to produce.

### 2.2. Mechanical design

The mathematical model directly inspires the mechanical design of the micromachined structure described in this paper. The design consists of two rectangular micromachined ducts separated by a thin membrane. Acoustic energy is injected at one end of the duct via a flexible partition, and propagates through the fluid, causing membrane motion at a location dependent on the frequency content of the input signal. To accomplish this, the properties of the central membrane: material, thickness, width, and support, along with functional variation of these properties, must be designed. In addition, duct geometry must be chosen along with terminating structures to allow acoustic energy injection, fluid filling, and static pressure release. Finally, a filling fluid must be selected. The goal is to create a mechanical sensor with the highest possible localization and sensitivity over the desired acoustic bandwidth, which can be practically manufactured and packaged using micromachining techniques.

Fabrication concerns suggest that the two-duct system be produced by etching through a silicon wafer. The membrane structure is also silicon (both single crystal and polysilicon membranes were fabricated). Material properties for silicon are taken to be: Young's modulus of 162 GPa, a density of 2330 kg/m<sup>3</sup>, and a Poisson ratio of 0.28.<sup>13</sup> Typical thickness

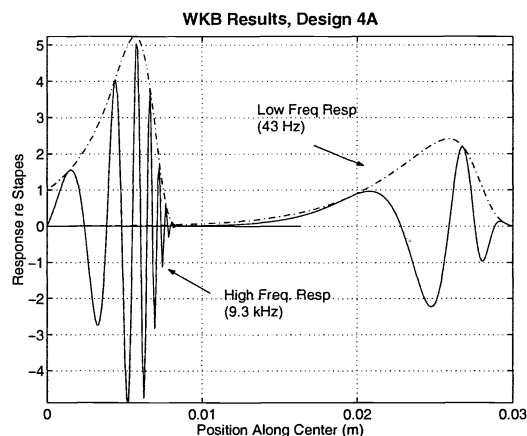


**Figure 2.** Example of typical WKB results for two separate input frequencies. Shown is the solution for plate displacement as a function of location along the plate centerline. Note that the low frequency excitation creates plate response at the wide end of the duct, while high frequency excitation localizes close to the narrow end. Acoustic energy is injected at  $x=0$  cm.

for a silicon wafer is  $500\text{--}525\ \mu\text{m}$ , which sets the duct height. Duct length is 3 cm, based on dimensions of the physical cochlea, and the ability to produce a reasonable number of devices (10 per wafer), while leaving ample room for 60 channels of output (with pad center spacing of 1 mm, two rows). The membrane property which can be most easily varied is the width. Functional variation of the membrane width from its initial narrow width to final width is exponential, which results in a log frequency to linear position mapping. WKB results indicate that a functional variation of the form  $b = b_0 e^{\alpha \cdot x/L}$  gives the best linear relationship between the log of frequency and the  $x$ -position of localization, and also produces the narrowest localization. In order to create the membrane width variation, a stiff shelf of material is needed for support. The most practical way to accomplish this is to allow the duct width to follow the membrane width, with the membrane spanning the full duct width. Silicone oil is used for the fluid. It is an attractive choice because it is inert, safe, transparent to visible light, relatively inexpensive, and available in a wide range of viscosities. The densities of silicone oils are similar to that of water, between 0.8 and 1.1 specific gravities. These initial mechanical design decisions form the basis for the optimization procedure which is discussed in Section 2.4.

### 2.3. Piezoresistor design

Transduction of mechanical membrane motion into an electrical signal can be accomplished using piezoresistors fabricated into the membrane. Doped silicon is a piezoresistive material, so integration of piezoresistors into the device can be accomplished by selective shallow doping of the structural layer and appropriate metalization. For this application, piezoresistors will be restricted to the edges of the beam structure where the highest strains occur, and span multiple beams by meandering in and out, as shown in Figure 3.

Much work has been reported on thin piezoresistive strain sensors in cantilevers, predominantly for atomic force microscopy (AFM).<sup>14–17</sup> Ried et al<sup>16</sup> report  $0.34\ \mu\text{m}$  thick AFM cantilevers fabricated by ion implantation and rapid thermal annealing. This is the shallowest implanted piezoresistor reported in the literature, to the best of this author's knowledge. Other recent work by Harley<sup>17</sup> reports piezoresistive AFM cantilevers with total thicknesses of  $90\ \text{nm}$  ( $\approx 0.1\ \mu\text{m}$ ). Harley's processing involves epitaxial growth of boron-doped thin films, which is not a readily available process at our facility. Hence, the thinnest possible membrane structure that can be achieved is  $0.34\ \mu\text{m}$ , using Ried's process for piezoresistor fabrication.

Optimization of the piezoresistors involves choice of two parameters: the fractional length of the beam which will be occupied ( $L$  in Figure 3), and the number of beams a particular channel spans (2 beams in Figure 3). These parameters can be varied to produce the greatest signal to noise ratio for a given membrane motion. For a comprehensive discussion of competing noise effects in a similar device, see the work done by Harley and Kenny<sup>18</sup> on piezoresistive AFM probes.

An iterative optimization procedure utilizing WKB results, a SUPREM process simulation doping profile, and piezoresistor noise models was carried out. From these results, the optimal number of beams per piezoresistor and the optimal

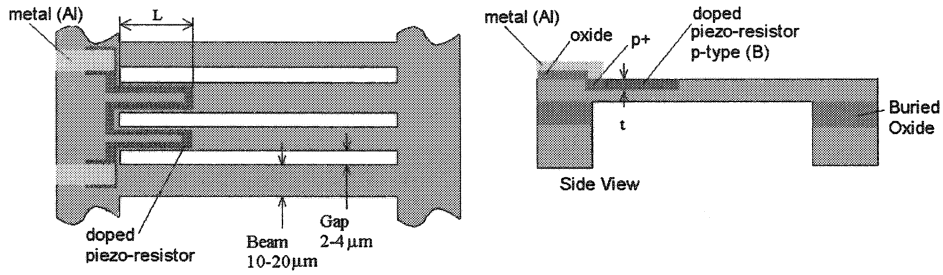


Figure 3: Piezoresistor geometry.

length of the piezoresistor are computed at each channel location along the device. Figure 4 gives an example of the optimization procedure. For this particular channel, best results are achieved by spanning 15 beams, and utilizing 15 % of the beam length. For this design, the major noise source is expected to be the external electronics. Improvement of device performance will be directly affected by the quality of the off-chip signal conditioning electronics.

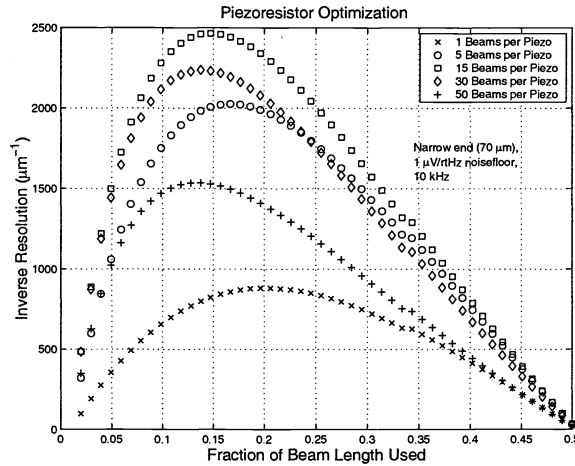


Figure 4. Examples of an optimization procedure result for a particular piezoresistor channel. Optimal values for both fractional beam length (0.15) and number of beams (15) are found for this channel.

#### 2.4. Mechanical Optimization

Five parameters remain for use in optimizing the mechanical design: initial and final membrane width, membrane thickness, and fluid density and viscosity. The aim is to maximize sensor resolution and the sharpness of acoustic localization in a desired frequency range. First, membrane width is chosen to achieve the desired frequency band. WKB modeling with fluid viscosity set to 0.01 Pa·s and fluid density set to 0.936 g/cm<sup>3</sup>, and with membrane thickness set to 0.34 μm gives a starting place for the designs: a 20 Hz - 20 kHz band device with a 0.34 micron thick strongly orthotropic silicon membrane requires duct width to vary from 70 μm to 1500 μm. From this point, the other parameters can be varied to improve performance while maintaining the responsive frequency band.

Piezoresistor sensitivity in ppm/μm is directly related to the average strain in the doped layer. The strain for a given membrane center displacement,  $\delta$ , goes as  $\delta \bar{y} \cdot b^{-2}$ , where  $\bar{y}$  is the center depth of the doping layer, equal to half the membrane thickness, and  $b$  is membrane width. Hence, to optimize piezoresistor output, it is necessary to maximize  $\delta \cdot \bar{y}/b^2$ . Computations of this quantity, as well as the strength of acoustic localization as measured by the width of the

frequency peak, were carried out at various frequencies for different values of the membrane thickness and fluid viscosity. Figure 5 is a typical result for resolution and localization strength at an intermediate excitation frequency of 177 Hz.

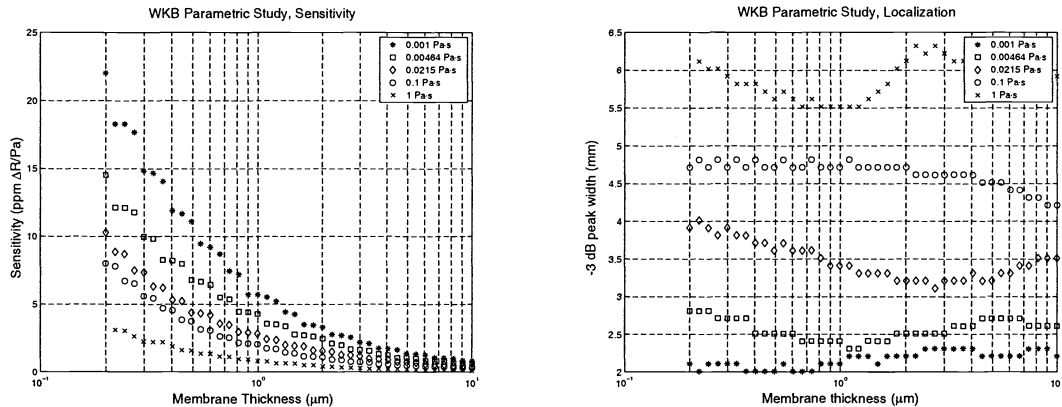


**Figure 5.** Structural optimization example: (a) Predicted sensitivity at 177 Hz peak referenced to ambient acoustic pressure, assuming a massless membrane between the fluid and the outside air. (b) -3 dB width of 177 Hz peak with various parameter values.

From these results, it can be seen that higher viscosities reduce the transducer sensitivity, as expected, and also decrease the acoustic localization. Thus, it seems best to select a low viscosity fluid. The lowest viscosity silicone oil available from Sigma-Aldrich has a viscosity of 0.006 Pa·s and a density of 0.962 g/cm<sup>3</sup> (Silicone oil AS 4). Another option is Clearco pure silicone fluid at 0.02 Pa·s. Decreasing membrane thickness has little effect on localization, but improves device sensitivity. Hence, the thinnest possible membrane is considered optimal. The minimum thickness is determined by achievable piezoresistor fabrication processes to be 0.34 μm (see Section 2.3). Variation of the fluid density (not shown in the graphs) between 1.1 g/cm<sup>3</sup> and 0.75 g/cm<sup>3</sup> has only a small effect on the results.

## 2.5. Orthotropy

The basilar membrane in the biological cochlea has orthotropic qualities; it is much stiffer in the transverse direction than the longitudinal direction. This feature reduces structural coupling of waves down the plate, and so most of the coupling between different locations is achieved through interaction with the surrounding fluid. This significantly increases acoustic localization. For this reason, it is desirable to produce a membrane structure with strong orthotropic qualities. At the macroscale this can be accomplished with composite materials, as described by Dodson.<sup>3,19</sup> However, at the microscale no such materials are currently available. Instead, using micromachining techniques, a very closely spaced array of many thin beams can be produced. Beam widths for the design discussed in this paper varied between 10 and 20 μm, with gaps between beams from 2 to 4 μm.

Two different models have been considered for the beam array plate. The first is to treat it as an orthotropic plate using WKB methods, as described in Section 2.1, while reducing the structural kinetic and potential energies by the proportion of structure to space. This method neglects viscous damping effects in the gaps, and pressure release effects associated with the gaps, but uses WKB to capture traveling wave phenomena and coupling. A second possibility is to consider the case of the isolated beam oscillating in an infinite viscous medium, as described by Kirstein et al.<sup>20</sup> This model neglects any communication between the beams through the fluid and the effects of wave propagation down the duct, but deals with the full viscous field correctly.

To verify the predictive capability of these models for beam array structures, a macroscale beam-array plate was fabricated using stereolithography. The plate was fabricated from 5170 Cibatool resin, with cured mechanical properties measured to be: Young's modulus=1.5 GPa, hysteretic damping parameter=0.18, density=1220 kg/m<sup>3</sup>. The plate is 1.3 mm thick and 165 mm long, and clamped into a brass two-duct system which linearly varies plate width from 3.4 mm to 25 mm. It has 109 separate beams, with beam width twice the width of the gaps between beams. Experiments were conducted using laser doppler vibrometry on this plate, operating in water, over a frequency range of 1-7 kHz. The results demonstrate agreement with the frequency-location mapping predicted by WKB and Kirstein models. A photograph of

the macroscale experimental setup is shown in Figure 6, along with a plot comparing predicted location of peak response from both models to experimental values. For comparison with experiment, peak location has been defined as position weighted by the displacement amplitude,  $W(x)$ ,

$$x_{peak} = \frac{\int_0^L W(x) \cdot x dx}{\int_0^L W(x) dx} \quad (1)$$

This is a more consistent measure of peak response location in imperfect data than selecting the point of maximum response. The results shown in Figure 6 employ this definition of peak location. For the Kirstein model, simply-supported boundary conditions were used on the beams, whereas for WKB a more complex modeshape incorporating the flexibility of the support structure was employed.<sup>19</sup>

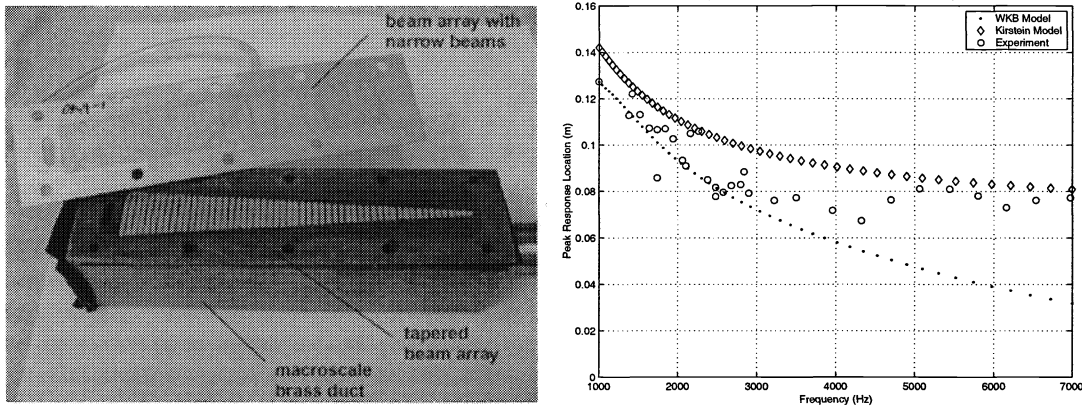


**Figure 6.** (a) Photograph of macroscale model. Total duct length is 200 mm. (b) Modeling and experimental results demonstrating correct prediction of frequency-location map.

### 2.6. Design Summary

Based on the discussed design goals, fabrication concerns, optimization study, and orthotropy results, three micromechanical designs are proposed targeting three frequency bands. Table 1 summarizes the designs. In all cases, the duct height is the wafer thickness, 525  $\mu\text{m}$ , and duct length is 3 cm. The membrane taper and duct width are exponential with functional form  $b = b_0 e^{\alpha \cdot x}$ . The structural layer spanning the duct is either single-crystal silicon or polysilicon, and consists of an array of beams between 10  $\mu\text{m}$  and 20  $\mu\text{m}$  wide, with gaps between beams of from 2 to 4  $\mu\text{m}$ . Fluid is pure silicone oil available from Clearco with a viscosity of 0.02 Pa·s.

Design	4A	4B	4C
Bandwidth	20 Hz - 20 kHz	100 Hz - 5 kHz	200 Hz - 10 kHz
BM Thickness ( $\mu\text{m}$ )	0.34 $\mu\text{m}$	0.34 $\mu\text{m}$	0.34 $\mu\text{m}$
BM Min Width ( $\mu\text{m}$ )	70 $\mu\text{m}$	140 $\mu\text{m}$	100 $\mu\text{m}$
BM Max Width ( $\mu\text{m}$ )	1800 $\mu\text{m}$	1000 $\mu\text{m}$	800 $\mu\text{m}$

**Table 1:** Major Designs Summary

## 3. FABRICATION

### 3.1. Process overview

The goal of the fabrication process is to produce the previously described structure. Optical sensing of membrane motion will be used, so the membrane must be accessible for optical measurement. An acoustic input structure must also be

realized, and the necessary structures to allow injection of the silicone oil. In addition, the processing steps must be compatible with (indeed, designed to facilitate) the doping process necessary to create the piezoresistors. However, the piezoresistor fabrication process will not be described here as it has not yet been perfected.

The mechanical portion of the devices have been fabricated out of both single crystal silicon and polysilicon. For the single crystal silicon devices, the starting wafers are 100mm, 525  $\mu\text{m}$  thick  $\langle 100 \rangle$  SIMOX SOI wafers from SOITEC, with a 3400  $\text{\AA}$  thick device layer and 4000  $\text{\AA}$  buried oxide. Both the handle and device layer are initially doped p-type to a resistivity of 14-22  $\Omega\cdot\text{cm}$ . The polysilicon devices are fabricated starting with 500  $\mu\text{m}$  thick  $\langle 100 \rangle$  100 mm single crystal silicon wafers initially doped p-type to a resistivity of 13  $\Omega\cdot\text{cm}$ . Fabrication proceeds according to the following process:

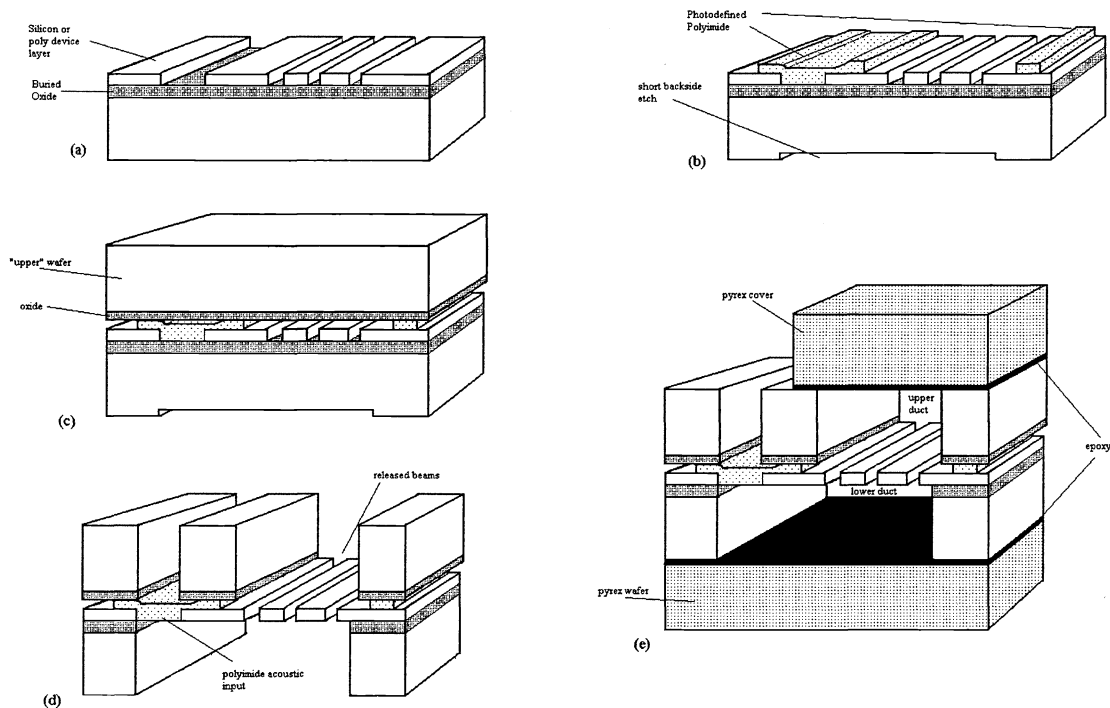


**Figure 7.** Fabrication process for mechanical structure. Steps refer to processing steps listed in the text below. (a) After RIE in step 3. (b) After polyimide spin and develop, step 5. (c) After upper wafer bond, step 6. (d) After through-etches and release, step 10. (e) After epoxy bonding of Pyrex covers, step 11.

### Process Steps

1. For polysilicon devices, deposit 4000  $\text{\AA}$  LPCVD oxide at 920  $^{\circ}\text{C}$ , 400 mtorr. Deposit 3400  $\text{\AA}$  LPCVD low stress polysilicon, 588  $^{\circ}\text{C}$ , 100 mtorr. Expected residual stress in polysilicon is 50-100 MPa.
2. For all wafers, 920  $^{\circ}\text{C}$ , 45 min. LPCVD oxide (1000  $\text{\AA}$  ). Implant Phosphorus through oxide with dose= $3.4 \cdot 10^{11}$  ions/ $\text{cm}^2$ , and energy=150 keV to create n-type background for piezoresistor isolation. 1 hour 920  $^{\circ}\text{C}$  anneal. Strip implantation oxide in BHF. Oxide deposition and anneal may help reduce residual stress. (See Section 3.4)
3. Etch beam pattern through 3400  $\text{\AA}$  device layer using  $\text{SF}_6$  RIE, masked with Shipley 1813 resist.

4. Protect frontside, remove backside silicon and oxide using RIE and Buffered HF. 8  $\mu\text{m}$  DRIE etch from backside using backside aligned duct mask (Shipley 1827 resist) to produce alignment pattern.
5. Spin on PI2731 (HD Microsystems) polyimide at 1 krpm. Softbake and photodefine to create adhesive pattern.
6. Adhesively bond device wafer using polyimide, topsides in, to prepared "upper" wafer, which is a starting wafer with 8000  $\text{\AA}$  of LPCVD oxide deposited on its topside. This is done on a hotplate at 300  $^{\circ}\text{C}$  for 3 hrs (1 hr. ramp up), at atmospheric pressure, with an applied mechanical bonding pressure of 60 kPa.
7. DRIE through-etch from backside of "upper" wafer to define upper duct structure, using STS multiplexed ICP tool. Etch mask is AZ9260 resist spun at 1 krpm. Etch stop is oxide on topside of "upper" wafer. See Section 3.2.
8. Mount etched side of wafer stack to a handle wafer with Shipley 1827 resist. Through etch lower duct pattern with identical DRIE recipe as in step 7. AZ9260 mask is used. Etch stop is buried oxide.
9. Strip resist in PRS2000 resist stripper, to separate handle wafer and remove masking resist (also requires short  $\text{O}_2$  plasma ash). Careful rinse in quiescent DI water and isopropyl alcohol.
10. 1:1 49%HF:DI water release, 5 mins. Careful rinse in quiescent DI water and isopropyl alcohol. 6 hour acetone soak to remove resist residues. See Section 3.4.
11. Adhesively bond backside Pyrex wafer using epoxy. Manually align diced Pyrex covers (35 mm x 9 mm) and epoxy bond in place. Inject silicone oil with syringe, and seal injection site and airholes with epoxy. See Sections 3.3 and 3.5.

### 3.2. Through wafer etching

The duct structure is micromachined by through-wafer etching the process wafers from the backside using an STS Multiplexed ICP (inductively coupled plasma) DRIE (deep reactive ion etch) tool. Characterization of a similar tool was carried out by Ayon, et al.,<sup>21</sup> where the effect of process parameters on etch rate, selectivity, anisotropy and uniformity are examined. For this application, it is important that the uniformity of the etch and selectivity to oxide are such that the through-wafer etch can be completed and the pattern cleared without etching through the etch stop and damaging the underlying structure.

A multiplexed recipe with a 13 sec etch, 160 sccm  $\text{SF}_6$ , 27 mtorr, 20.5 W platen power, 800 W coil power alternating with 7 sec 80 sccm  $\text{C}_4\text{F}_8$  passivation at 17 mtorr, 600 W coil power was used. Measurements demonstrated an average etch rate of 3.6  $\mu\text{m}/\text{min}$  for silicon, with a loading of between 4 and 18 % (depending on the pattern), and minimum feature size of 70  $\mu\text{m}$ . Selectivity to the LPCVD oxide was 270:1. Etch uniformity across the wafer was 11%. Uniformity and selectivity are sufficient to allow the through-etch to stop on a 4000  $\text{\AA}$  buried oxide, while clearing all patterns. Some difficulty was encountered in opening the narrowest features (70  $\mu\text{m}$ ), particularly near the center of the wafer.

### 3.3. Wafer bonding

Wafer bonding was accomplished using adhesive bonding techniques, which allow low temperature full wafer bonding, and can be applied to surfaces with a wide variety of surface materials and topology. Polyimide was used as a photodefinable adhesive between the two main device wafers. It was found to be very effective and easy to work with. A 300  $^{\circ}\text{C}$  cure on a hotplate for 3 hours with 60 kPa of applied pressure produced a strong bond. Since the polyimide was readily photodefinable, a sealing "ring" could be defined around each duct, producing a good seal while ensuring that no adhesive interfered with the mechanical structure. The choice of curing time and mechanical pressure was motivated by Niklaus et al.,<sup>22</sup> whose work characterizes bonds with a number of different adhesives.

Outer bonding of Pyrex cover wafers and cover slips was accomplished with epoxy. A thermally cured epoxy, 377 from EpoTek, was used for the full wafer bond to the backside of the device structure. The epoxy was mixed and spun on to the Pyrex wafer at 1000 rpm. Initial wetting of the Pyrex was poor, so it was important to quickly place the device wafers into contact or the epoxy would form droplets. However, the epoxy did wet the silicon surface well. After a 150  $^{\circ}\text{C}$  cure for 60 mins, the bond was fully established. Bonding was attempted both with and without mechanical clamping pressure. No advantage was derived from using mechanical clamping pressure. In both cases, the bond was strong and

the seal was good. Voids were present, but about 90% of the wafer surface was bonded, sufficient for hermetic sealing. It was helpful to manually press the wafers together at many points to initially wet the wafer surface. Using this process, hermetic full wafer adhesive bonds have been achieved.

Two major problems were encountered when using the thermal epoxy for full wafer bonding. Due to the ease with which the epoxy wets the silicon surface, epoxy was pulled into narrow through-wafer features, particularly at the narrow duct ends, and plugged the duct, as shown in Figure 8. This is unavoidable if the entire wafer is coated with epoxy and narrow features are open to the epoxy. To avoid this, it will be necessary to selectively apply small amounts of epoxy far enough away from the features that it will not be pulled into the trenches. A second problem was encountered with deposition of evaporating epoxy solvents on the membrane structure.

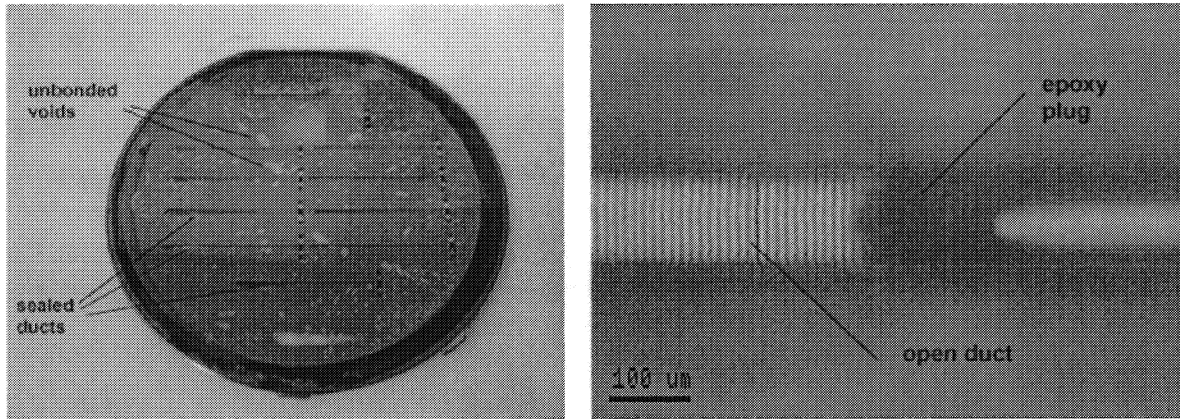


**Figure 8.** Epoxy wafer bonding. (a) Full wafer thermal epoxy bond showing 90 % coverage and voids. Wafer shown is 100mm in diameter. (b) Micrograph showing epoxy duct clogging.

The upper Pyrex covers (6mmx31.5mm) were diced out of a Pyrex wafer and bonded to the upper side of the device wafer using EZ-Lam epoxy laminate available from Aerospace Composite Products. In this case, thin lines of the epoxy were manually deposited at the edges of the covers using a thin wire applicator. When the covers were placed in contact with the wafer, the epoxy traveled along the interface to create a strong, large area bond. By depositing the correct amount of epoxy, it was possible to avoid duct filling. This epoxy cures at room temperature, avoiding heating. The EZ-Lam epoxy, applied manually, was superior to EpoTek 377 for this application, avoiding duct clogging and residue deposition.

Two other techniques for wafer bonding were considered. Fusion bonding allows silicon to silicon bonding, but requires high temperatures and flat surfaces. Due to the desire for compatibility with a shallow piezoresistor (see Section 2.3), and topology of metal lines, fusion bonding was not deemed practical. Anodic bonding allows bonding of Pyrex to silicon, utilizing somewhat elevated temperatures and electrostatic attraction between the materials.<sup>13</sup> This process could potentially be used for the outer cover bonds described in this paper, although it could not be used for the silicon to silicon bonding at the device wafer interface.

### 3.4. Release

Final structure release is accomplished using 1:1 49% HF:DI water oxide etch. This etch removes the buried oxide and the oxide on the inner side of the “upper” device wafer, releasing the silicon beam structure. The structure is fully released in 5 minutes. Due to the double-sided duct, the etchant can easily remove oxide from both sides of the beams. As the beams are suspended over the duct cavity, there is no concern about stiction during drying. Suspended beam array structures 3400 Å thick have been released by this process. Figure 9 shows examples of successfully released structures.

There are challenges associated with the release step. First, the structure is extremely fragile, due to beam thickness of 3400 Å, and lengths of up to 1.5 mm. Thus, any macroscopic mechanical loading will fracture all beams. For this reason, it is critical that during and after release the wafers are never subjected to a circulating rinse, spin dry, or nitrogen gun dry.

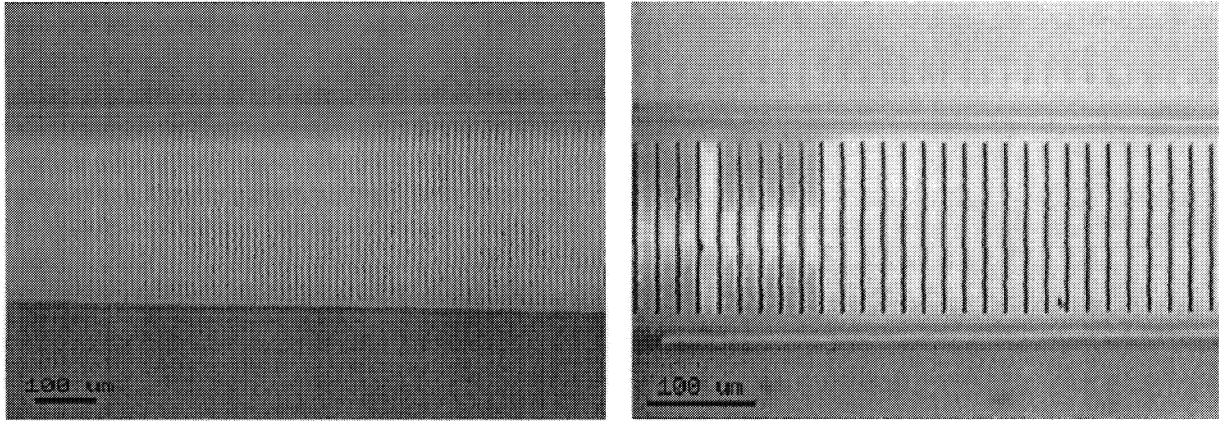


**Figure 9.** Successfully released beam structures. (a) Device 4B-1, released beam structure viewed through sealed Pyrex lid and silicone oil filled cavity. (b) Device 4B-2 released beams viewed prior to sealing and filling operations.

The devices must be rinsed carefully in quiescent baths, and allowed to air dry in atmosphere. A final isopropyl alcohol rinse prior to atmospheric drying was effective in promoting rapid drying.

A second issue is less catastrophic beam failure, observed forms of which included beam buckling and a twist-stick mode. Long beams in all but one device (out of 15) buckled. Figure 10 (a) shows a micrograph of the onset of buckling. The buckling length was measured, and was similar for all devices, for both polysilicon and SOI wafers, varying between 350  $\mu\text{m}$  and 1 mm. Average length for the onset of buckling was 490  $\mu\text{m}$  for the polysilicon devices, and >570  $\mu\text{m}$  for the SOI devices (one device had no visible buckling for beams up to 1mm in length). See Figure 11 for a full report. It is interesting to note that the polysilicon devices did not exhibit a significantly shorter buckling length, despite the expectation that the LPCVD polysilicon would have a higher residual stress than the SIMOX SOI device layer.

From the critical buckling length,  $L$ , the residual strain in the device layer can be estimated from <sup>23</sup>

$$\sigma_{crit} = \frac{4\pi^2 EI}{L^2 A} = \frac{\pi^2 E h^2}{3L^2} \quad (2)$$

where  $\sigma_{crit}$  is the critical strain required to buckle a rectangular clamped-clamped beam. For  $E=162$  GPa,  $h=0.34$   $\mu\text{m}$ ,  $L=490$   $\mu\text{m}$ , equation 2 estimates a compressive residual stress of 0.26 MPa in the polysilicon structural layer. Process characterization for the polysilicon device layer predicts an as-deposited residual stress of 50-100 MPa. <sup>24</sup> It is likely that the high temperature oxidation (920°C, 45 min) and anneal (920°C, 1 hour) step conducted after film deposition reduced the residual stress, but further study is needed to verify this. In order to avoid buckling issues, it may be necessary to produce a design with shorter beams. In addition to buckling, the longest beams sometimes twisted and stuck together, as seen in Figure 10 (b). This failure mode could potentially be avoided by using a critical point drying method.

### 3.5. Filling and sealing

Filling of the fabricated devices was accomplished by using a syringe to inject Clearco pure silicone oil (0.02 Pa·s viscosity) through a micromachined needle port at one end of the duct. Air holes were micromachined at the other end of the duct, so that injected silicone oil could force air out and fill the device. The silicone oil wetted the silicon surface of the duct well, and no bubbles were observed during or after the filling process. In this application, the narrow ducts seem to be effective at suppressing bubble formation by pulling the fluid in via surface forces. Once the silicone oil is injected, the devices are sealed with epoxy over the needle port and air holes.

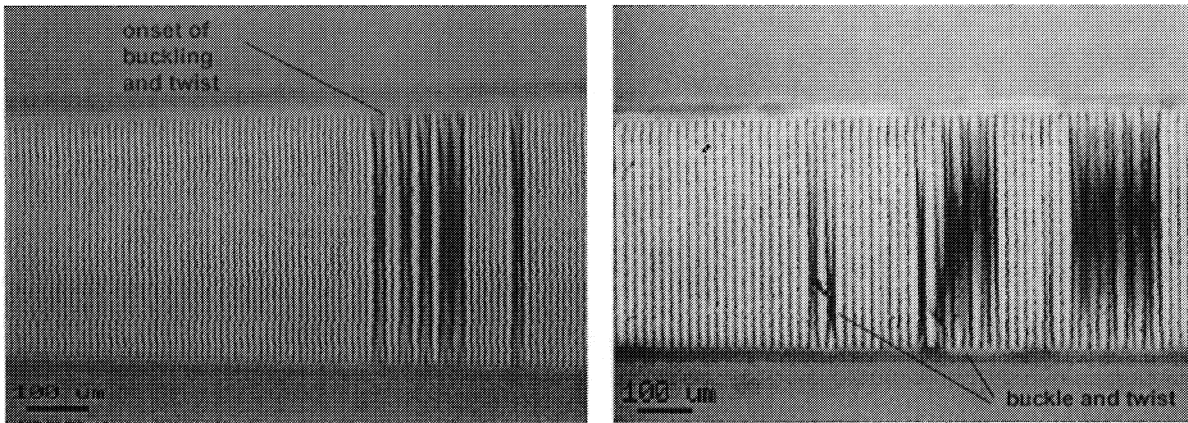


Figure 10: Released structure issues: (a) Buckling (b) Twist-stick

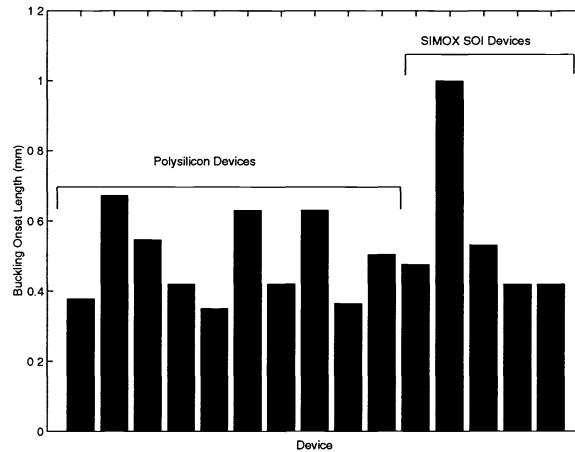


Figure 11: Measured buckling length.

#### 4. CONCLUSIONS

Design efforts aimed at producing a MEMS cochlear-like transducer have been detailed. This work was based around WKB (Wentzel-Kramer-Brillouin) approximate techniques for cochlear modeling. Features of an optimal transducer design were presented, including a specific design example. A beam array structure which captures the orthotropic qualities of the biological basilar membrane was suggested, with mathematical modeling and macroscale experimental results indicating effectiveness.

A full fabrication process for the mechanical structure was presented. Particular challenges related to through wafer etching, adhesive wafer bonding, structure release and device filling were discussed. It was demonstrated that the process is practical for constructing cochlear-like acoustic sensors of this type. Potential difficulties associated with structural failure, etch uniformity, and adhesive flow were emphasized.

Additional work will be conducted to measure the response of these micromachined structures in the laboratory. Piezoresistive transduction elements will also be integrated with the mechanical structure to produce a functioning sensor system. Successful operation of such a device offers potential benefits in understanding cochlear mechanics, and will also allow further exploration of this novel and effective acoustic transduction technology. Addition of active components to this design will allow experimental investigation of active cochlear models, which are being developed to account for improved cochlear response characteristics observed in living subjects.

## ACKNOWLEDGMENTS

We would like to acknowledge the financial support of the Office of Naval Research and the National Science Foundation. In addition, we are grateful to Profs. Nguyen, Najafi, and Kurabayashi, and to David Lemmerhirt, for their assistance.

## REFERENCES

1. P. Dallos, A. Popper, and R. Fay, *The Cochlea*, vol. 8 of *Springer handbook of auditory research*, Springer, New York, 1996.
2. A. A. Parthasarathi, *Numerical modeling and electro-acoustic stimulus response analysis for cochlear mechanics*. PhD thesis, University of Michigan, 2000.
3. J. Dodson and K. Grosh, "Cochlear-based transducer designs," in *Proceedings of the ASME, Noise control and acoustics division*, **26**, pp. 383–385, 1999.
4. K. Tanaka, M. Abe, and S. Ando, "Novel mechanical cochlea fishbone with dual sensor/actuator characteristics," *IEEE/ASME Transactions on Mechatronics* **3**, pp. 98–105, 1998.
5. M. Harada, N. Ikeuchi, S. Fukui, and S. Ando, "Fish-bone structured acoustic sensor toward silicon cochlear systems," in *Proceedings of the SPIE, SPIE Conference on Micromachined Devices and Components IV* **3514**, pp. 266–275, 1998.
6. D. Haronian and N. C. MacDonald, "A microelectromechanics-based frequency-signature sensor," *Sensors and Actuators A* **53**, pp. 288–298, 1996.
7. K-M. Lim, A. M. Fitzgerald, C. R. Steele, and S. Puria, "Building a physical cochlea model on a silicon chip," *Recent developments in auditory mechanics meeting in Sendai, Ja.*, 1999.
8. C. R. Steele and L. A. Taber, "Comparison of wkb calculations and experimental results for three-dimensional cochlear models," *J. Acoust. Soc. Amer.* **65**, pp. 1007–1018, 1979.
9. E. de Boer and M. A. Viergever, "Validity of the liouville-green (or wkb) method for cochlear mechanics," *Hearing Research* **8**, pp. 131–155, 1982.
10. G. Zhou, L. Bintz, D. Z. Anderson, and K. E. Bright, "A life-sized physical model of the human cochlea with optical holographic readout," *J. Acoust. Soc. Am.* **93**, pp. 1516–1523, 1993.
11. G. von Békésy, *Experiments in Hearing*, McGraw-Hill, New York, 1960.
12. A. A. Parthasarathi, K. Grosh, and A. L. Nuttall, "Three-dimensional numerical modeling for global cochlear dynamics," *J. Acoust. Soc. Amer.* **107**, pp. 474–485, 2000.
13. G. Kovacs, *Micromachined Transducer Sourcebook*, McGraw-Hill, New York, 1998.
14. B. W.-H. Chui, *Advanced Silicon Micromachined Cantilevers for Atomic Force Microscope Data Storage*. PhD thesis, Stanford University, 1998.
15. M. Tortonese, R. C. Barrett, and C. F. Quate, "Atomic resolution with an atomic force microscope using piezoresistive detection," *Applied Physics Letters* **62**, pp. 834–936, 1993.
16. R. P. Ried and L. S. Fan, "6-mhz 2-n/m piezoresistive atomic-force-microscope cantilevers with incisive tips," *Journal of Microelectromechanical Systems* **6**, pp. 294–302, 1997.
17. J. A. Harley, *Advances in Piezoresistive Probes for Atomic Force Microscopy*. PhD thesis, Stanford University, 2000.
18. J. Harley and T. Kenny, "1/f noise considerations for the design and process optimization of piezoresistive cantilevers," *Journal of Microelectromechanical Systems* **9**, pp. 226–235, 2000.
19. J. Dodson, *Efficient finite element methods/reduced-order modeling for structural acoustics with applications to transduction*. PhD thesis, University of Michigan, 2000.
20. S. Kirstein, M. Mertesdorf, and M. Schonhoff, "The influence of a viscous fluid on the vibration dynamics of scanning near-field optical microscopy fiber probes and atomic force microscopy cantilevers," *Journal of Applied Physics* **84**, 1998.
21. A. A. Ayon, R. A. Braff, C. C. Lin, H. H. Sawin, and M. A. Schmidt, "Characterization of a time multiplexed inductively coupled plasma etcher," *Journal of The Electrochemical Society* **146**, pp. 339–349, 1999.
22. F. Niklaus, P. Enoksson, E. Kalvesten, and G. Stemme, "Low-temperature full wafer adhesive bonding," *Journal of Micromechanics and Microengineering* **11**, pp. 100–107, 2001.
23. W. Fang, C.-H. Lee, and H.-H. Hu, "On the buckling behavior of micromachined beams," *Journal of Micromechanics and Microengineering* **9**, pp. 236–244, 1999.
24. U. of Michigan, "Internal solid state electronics lab mems exchange documentation." 2002.